

Exploring the Stability of Twisted van der Waals Heterostructures

Andrea Silva,* Victor E. P. Claerbout,* Tomas Polcar, Denis Kramer, and Paolo Nicolini



Cite This: ACS Appl. Mater. Interfaces 2020, 12, 45214–45221



Read Online

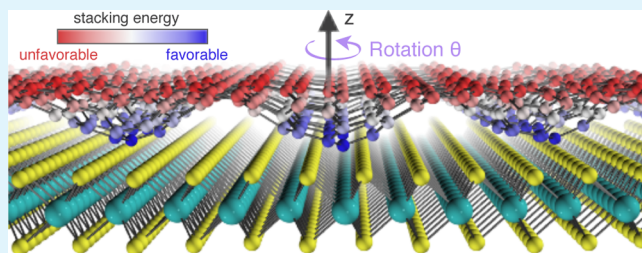
ACCESS |

Metrics & More

Article Recommendations

Supporting Information

ABSTRACT: Recent research showed that the rotational degree of freedom in stacking 2D materials yields great changes in the electronic properties. Here, we focus on an often overlooked question: are twisted geometries stable and what defines their rotational energy landscape? Our simulations show how epitaxy theory breaks down in these systems, and we explain the observed behavior in terms of an interplay between flexural phonons and the interlayer coupling, governed by the moiré superlattice. Our argument, applied to the well-studied MoS₂/graphene system, rationalizes experimental results and could serve as guidance to design twistronic devices.



KEYWORDS: heterostructures, molybdenum disulfide, graphene, twist deformation, molecular dynamics simulations, twistronics

INTRODUCTION

van der Waals (vdW) 2D materials, such as graphite and the family of transition metal dichalcogenides (TMDs), are a class of compounds characterized by an anisotropic structure. Strong intralayer covalent bonds complement the weak vdW interlayer interactions, which facilitate the lamellar structure of bulk crystals. Because of their diverse chemistry and versatile properties, these materials have received significant attention from the scientific community in the past decades.^{1–3} Applications can be found in microelectronics,^{4,5} catalysis,^{6–8} and tribology.^{9,10} Although the attractive properties of the pure compounds are widely known, recent efforts have been focusing on the physics and properties emerging from the stacking degree of freedom offered by these lamellar materials. Different types of single layers can be mixed and matched to create new superstructures, termed *heterostructures*.^{11–14} A key feature, affecting the behavior of multilayered structures, is the relative orientational mismatch between layers. Although heterostructures are intrinsically incommensurate because of the different lattice constants of the parent single layers, incommensurability can also arise in homostructures because of a relative misalignment of the single layers.⁹

The relative mismatch between layers, both for homo- and heterostructures, has been related to a range of electronic and mechanical properties.^{9,15–20} A flourishing new branch in the field of condensed matter, known as *twistronics*, promises to allow fine-tuning of the electronic properties using the rotational misalignment between layers.^{17,21} A notable example is the recent discovery of unconventional superconductivity in bilayer graphene (G) twisted at a *magic angle* of 1.1°.²¹ Another study found that the vertical conductivity of bilayer MoS₂/G heterostructures varies by a factor of five when imposing an angle of 30° between the layers.²² Finally, a

pioneering work⁹ showed that by switching from commensurate to incommensurate orientation in graphite systems, it is possible to achieve a state in which the coefficient of friction vanishes, the so-called *superlubric* regime.

Despite the interesting physics, which results from these relative mismatches, an often overlooked question is by what their rotational energy landscape is determined and thus which geometries are stable. Indeed, experimental studies are contradictory on this point, with a wide range of misfit angles found, even for the same type of system.^{23–26} Below, we give a few examples of heterostructures based on MoS₂ on G. This system may be regarded as the prototypical 2D heterostructure, as it combines two well-known and extensively studied materials, widely reported in the literature. Moreover, it has been reported that MoS₂/G heterostructures show interesting electronic behavior as a function of their mismatch angle.^{27,28} Using chemical vapor deposition (CVD), Liu *et al.* epitaxially grew triangles of MoS₂ on top of G, about 0.135 μm in size, with the majority of them (84%) aligned to the substrate and the remainder rotated by 30°.²³ Using the same technique, Shi *et al.* found mismatch angles between MoS₂ and G, on top of a Cu foil, ranging from -11 to 18°, with hexagonal flake sizes of about 1 μm.²⁴ For CVD-grown flakes of 9 μm, Lu *et al.* found a mismatch with typical angles below 3°.²⁵ Finally, using an exfoliation protocol, Adrian *et al.* prepared multilayered heterostructures and observed a misfit

Received: August 3, 2020

Accepted: September 8, 2020

Published: September 8, 2020



angle of 7.3° .²⁶ In addition to different values for the observed mismatch angle, these studies offer different explanations for its origin. Although some attribute the observed (mis)alignment to the vdW epitaxy, accommodating the mismatch in lattice constants,^{23,24} others use the structural features of the underlying G and the edges²⁵ as an explanation.

In a recent theoretical work, Zhu *et al.*¹⁵ explained the orientational ordering of finite size homostructures, for example, MoS₂ flakes on a MoS₂ substrate, using a purely geometrical argument: the lowest energy configuration is the one obtained by the rototranslation of the rigid flake which maximizes the number of locally commensurate regions. Although this argument is solely based on geometry, it provides a satisfactory approximation for finite size systems but in the limit of infinite planes, that is, for large enough flakes, commensurate regions equal incommensurate ones. Therefore, in the limit of extended interfaces, other theoretical frameworks are needed.

In this contribution, we aim to explore the energy landscape originating from the rotational degree of freedom of edge-free, complex layered heterostructures and relate its fundamental origin to incommensurability and layer deformation at imposed angles. This will provide guidance for the design of vdW heterostructures and the control of the twisting degree of freedom. In order to make a more general point about the relative importance of different contributions, in determining the total energy landscape, we focus on a specific but well-studied system, namely, MoS₂/G. Although previous energy analysis focused on commensurate MoS₂/MoS₂ homostructures²⁹ or near-commensurate 2D-crystal G/hBN heterostructures,³⁰ the MoS₂/G BL system has a mismatch ratio $\rho = l/l \approx 0.8$ far away from the commensurate value $\rho = 1$ and, moreover, is composed of a mixture of 2D and 3D crystal monolayers. This analysis shows the practical application of our argument and will also allow us to comment on the apparently contradictory experimental observations regarding this particular system.

RESULTS AND DISCUSSION

In order to avoid finite-size effects and harvest information solely from the relaxation of the atoms in the layers, we implemented a protocol to build edge-free geometries. The resulting supercells are simultaneously compatible with the lattice mismatch and a relative imposed angle between the layers. As a result, periodic boundary conditions (PBCs) can be applied to these structures. The starting interface geometry is described by a pair of 2D lattices defined by vectors $(l_a \hat{a}_1, l_a \hat{a}_2)$ and $(l_b \hat{b}_1, l_b \hat{b}_2)$, where l_a and l_b represent the lattice constants and the \hat{b}_i vectors are rotated by an angle θ with respect to \hat{a}_i . Two layers will be compatible if they satisfy the matching condition $l_a(n_1 \hat{a}_1 + n_2 \hat{a}_2) = l_b(m_1 \hat{b}_1 + m_2 \hat{b}_2)$, where the integer numbers n_1 , n_2 , m_1 , and m_2 are supercell indices, representing the repetition along each lattice vector. In practice, for incommensurate lattice constants, the matching condition yielding PBC-compliant supercells can only be satisfied approximately, that is, the lattice spacing l' of one of the two components needs to deviate from its equilibrium value l . Here, in order to obtain suitable structures with imposed angles between 0 and 60° , we accept supercells satisfying $|l' - l| < 5 \times 10^{-7} \text{ \AA}$. The resulting strain is applied to the MoS₂ layer, which leads to a maximum strain $\epsilon = \frac{l' - l}{l}$ within the same order of magnitude, four orders less than

reported strains in other computational studies.^{31–33} This protocol yields a set of supercells, each of which has a different number of atoms of up to 343,893, created according to the four supercell indices resulting in a unique twisting angle, satisfying the matching condition. Details of this protocol and all the parameters of the supercells used are reported in the Supporting Information.

In these supercells, we distinguish intralayer and interlayer interatomic interactions, resulting in the following Hamiltonian

$$H = H_{L_1} + H_{L_2} + H_{L_1 L_2} \quad (1)$$

The G layer is modeled with the REBO potential,³⁴ $H_{L_1} = H_C^{(\text{REBO})}$, while the three-body Stillinger–Weber (SW) potential³³ is used for MoS₂, $H_{L_2} = H_{\text{MoS}_2}^{(\text{SW})}$. Interlayer coupling is described by the Lennard-Jones (LJ) potential

$$\begin{aligned} H_{L_1 L_2} &= H_{\text{C-Mo,C-S}}^{(\text{LJ})} \\ &= \sum_{i \in \text{C}} \sum_{j \in \text{Mo,S}} 4\epsilon_{ij} \left[\left(\frac{\sigma_{ij}}{r} \right)^{12} - \left(\frac{\sigma_{ij}}{r} \right)^6 \right] \end{aligned} \quad (2)$$

Because the interlayer interactions are especially relevant for the aim of this work, we refined the values for the C–Mo and C–S interactions found in ref 33. As a reference set, we computed the binding energy curves at the DFT level, using the Vienna Ab initio Simulation Package (VASP)^{35,36} within the projector augmented-wave (PAW) framework.³⁷ The exchange–correlation potential is approximated using the PBE functional,³⁸ and the vdW dispersion is described by the DFT-D2 method.³⁹ After this procedure, we are able to perform energy minimizations using the conjugate gradient algorithm available within the LAMMPS package.⁴⁰ More details about the fitting and minimization procedure can be found in the Supporting Information. An overview of the computational setup can be found in Figure 1.

An approximate theory for the orientational ordering of an incommensurate interface was proposed by Novaco and McTague.^{41,42} Although developed in the context of epitaxial growth of noble gas layers on metal surfaces, it has been successfully applied to the behavior of mesoscopic colloidal layers in optical lattices⁴³ and metal clusters adsorbed on G.⁴⁴ The assumption of the Novaco–McTague (NM) theory is that two purely 2D systems, linked *via* an interface, may be divided into two separate components: a soft adsorbate layer, treated within the harmonic approximation, atop a rigid substrate. This means that one of the intralayer terms in eq 1 is substituted by its harmonic approximation, while the coordinates of the second layer are frozen at its initial values, r_0 . For example, considering G as the adsorbate and MoS₂ as the substrate yields the following Hamiltonian

$$H_{\text{NM}} = H_C^{(\text{REBO})}|_{\text{harmonic}} + H_{\text{MoS}_2}|_{r_0} + H_{\text{C-MO,C-S}} \quad (3)$$

If the substrate and the adsorbate lattices are incommensurate, because of a mismatch in lattice constants, the system is frustrated: the intralayer interactions within the adsorbate favor the intrinsic equilibrium lattice spacing, while the interactions with the substrate drive the atoms away from their equilibrium positions. In the limit of long-wavelength distortions, the NM theory predicts that the system can lower its energy by converting part of the longitudinal stress coming from the

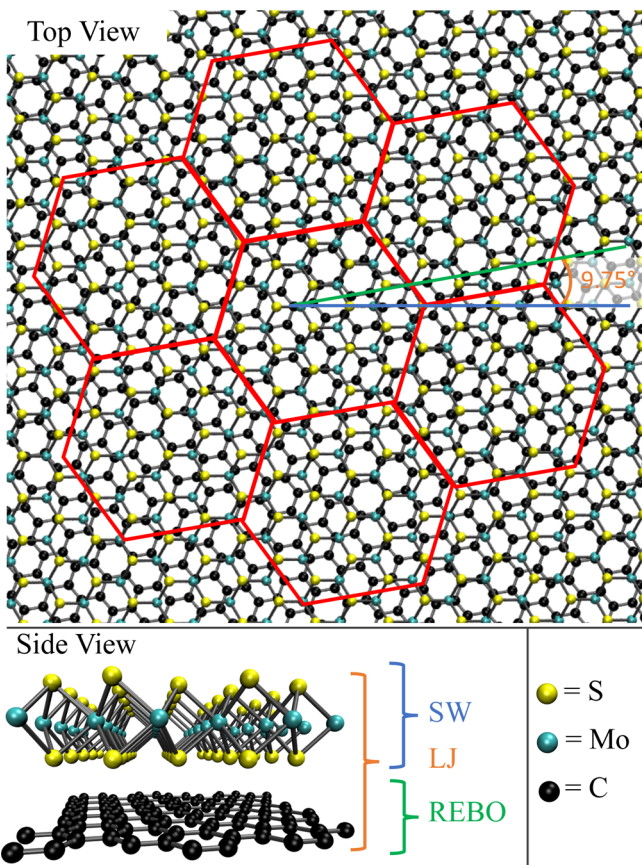


Figure 1. Schematic overview of the computational setup displayed for a mismatch angle of 9.75°. In the top panel, a top view is provided, including a sketch of moiré tiling resulting from the geometrical interference between the two lattices. The mismatch angle between the lattice direction of MoS₂ (blue line) and G (green line) lattices is reported as well. In the bottom panel, a side view is provided, including the corresponding force fields that have been used.

incommensurability into shear stress. This yields a small misalignment angle between the two lattices given by

$$\cos \theta_{\text{NM}} = \frac{1 + \rho^2(1 + 2\delta)}{\rho[2 + \delta(1 + \rho^2)]} \quad (4)$$

where $\rho = l_{\text{substrate}}/l_{\text{adsorbate}}$ is the mismatch ratio between the two lattices and $\delta = (c_L/c_T)^2 - 1$, with c_T and c_L being the transverse and longitudinal sound velocities of the adsorbate, respectively.

The result of NM in eq 4 can be applied to our system by extracting the sound velocity of each single layer from the phonon dispersion, as reported in the Supporting Information. There are two possible scenarios: G can be treated as the rigid substrate, while MoS₂ acts as a soft adsorbate or vice versa. In the first case, the theory predicts $\theta_{\text{NM}}^{\text{MoS}_2} = 8.0^\circ$, while if G is the adsorbate, the minimum-energy angle is $\theta_{\text{NM}}^G = 8.6^\circ$. The prediction of the NM model can be verified by minimizing the total energy of the twisted geometries described above under suitable constraints. We froze the atoms of the heterostructures in the direction perpendicular to the surface, that is, the z axis, effectively reducing the dimensionality of the system to 2D. Furthermore, we also froze the atoms of the substrate layer in the in-plane directions x and y, enforcing a fully rigid substrate.

As mentioned at the beginning of this section and explained in detail in one of the sections of the Supporting Information, the edge-free geometries used in this work inevitably retain a degree of stress resulting from the matching condition for the two lattices in order to be able to apply PBCs. The slightly different strains, unique to every geometry, result in different offsets in the obtained energies. Because these offsets are of the same order as the energy gain arising from in-plane displacement of the atoms, this residual strain leads to a significant noise in the signal of the energy profile as a function of the imposed angle. To overcome this problem and to obtain a clear signal from our simulations, we enhanced the LJ-coupling strength between the MoS₂ and G layers. In other words, we set the LJ parameters ϵ_{ij} in eq 2 to $\epsilon'_{ij} = 100 \epsilon_{ij}$ during geometry optimization. Next, the applied bias is corrected by scaling back the energy profile, as if simulated with the original value of ϵ_{ij} . As is shown in section three of the Supporting Information, this computational trick solely reduces the noise without affecting the actual physics of the problem.

Figure 2 shows the optimized energy E (meV/atom) as a function of the angle θ (°), with respect to the energy of the

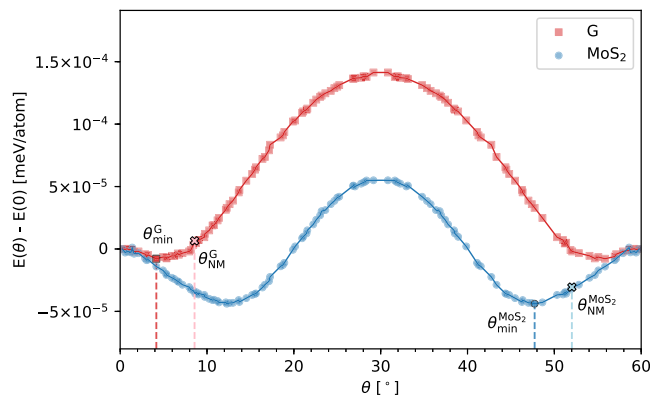


Figure 2. Energy E (meV/atom) as a function of the imposed angle θ (°) for different 2D models: red squares refer to flexible G on top of rigid MoS₂; blue circles refer to flexible MoS₂ on top of rigid G. The labels in the legend indicate the flexible ML. The reference value of the energy scale is set to $E(0)$. The minimum-energy point along each curve is highlighted by a dashed line and a label. Red and blue crosses (accompanied by a label) mark the minimum angle predicted by the NM theory for the first and second cases, respectively. The minimum-energy and NM-predicted angles for flexible MoS₂ are reported starting from 60° for easiness of reading.

aligned structures, $E(0)$. The two curves refer to the following models: 2D-adsorbed G atop rigid MoS₂ (red) and 2D-adsorbed MoS₂ atop rigid G (blue). Both cases reveal a minimum at a nonzero angle: for the adsorbed G case, the minimum is found at $\theta_{\text{min}}^G = 4.2^\circ$, while for the adsorbed MoS₂ case, it is at $\theta_{\text{min}}^{\text{MoS}_2} = 12.3^\circ$. Because of the intrinsic hexagonal symmetry of our system, each curve has two symmetrical minima centered at around 30°. The simulations show that the physics described by the approximation of eq 4 is still valid, that is, a nonzero minimum angle is observed for both cases. However, the absolute values of the predicted and observed angles are not in agreement, yielding a discrepancy of $\theta_{\text{min}}^G - \theta_{\text{NM}}^G = -4.4^\circ$, in the case of 2D-adsorbed G, and $\theta_{\text{min}}^{\text{MoS}_2} - \theta_{\text{NM}}^{\text{MoS}_2} = 4.3^\circ$, in the case of 2D-adsorbed MoS₂.

A previous study of G and h-BN heterostructures showed³⁰ that the NM model quantitatively describes the relaxation of the constrained system of these purely 2D materials. Here, the NM theory captures the basics of the physics but is not able to describe satisfactorily the complex geometry of the bilayer system, especially in the case of the flexible MoS₂ layer. We attribute the poor prediction of the theory in our case to the internal 3D structure of the MoS₂ monolayer, which indeed is unaccounted for in the NM model. This suggests that the NM theory is generally of limited utility for any bilayer comprising TMDs or other systems with a 3D monolayer structure. Another difference between our results and the results found for G/hBN heterostructures³⁰ is the quantitative difference in the energy values. In fact, our results report energy differences of 1 order of magnitude less. We explain this difference by the earlier mentioned relatively large MoS₂/G BL system mismatch ratio $\rho = l/l \approx 0.8$. Because of this significant incommensurability between the MoS₂ and G, present for all rotations, the atom displacements and energy differences are expected to be less pronounced. In fact, a similar observation has been carried out experimentally by Diaz *et al.*²⁷ and Pierucci *et al.*²⁸ For example, Diaz *et al.* found that the MoS₂/G moiré pattern obtained *via* AFM measurements was less pronounced compared to the one of hBN/G.

Considering another case, one in which all degrees of freedom are considered, that is, all atoms are free to move in the 3D space, the NM theory is even qualitatively inadequate. Figure 3 shows the energy E (meV/atom) as a function of the

(0°,60°) toward the global maximum at a mismatch angle of 30°. From Figure 3, one can thus deduce that at 0 K, the fully flexible bilayer system will be stable when aligned at 0 or 60°. The energy profile around a misalignment of 30° is flat, and the misaligned geometry at this angle could therefore be characterized as metastable, as a vanishing force $F = -dE(\theta)/d\theta$ drives the system toward the global minima at 0 or 60°. In the thermodynamic limit, this orientation should not occur, considering it is the global energy maximum. The fact that nonaligned structures are observed experimentally²³ can be explained by the fact that this type of geometry can be temporarily stabilized by a small internal friction, for example, because of local defects, creating energy barriers that need to be overcome first.

The NM theory does not hold when structural distortions perpendicular to the interface are allowed. Our results indicate that these are important for MoS₂/G heterostructures, and we believe that this is also the case for other complex heterostructures. The core of the NM argument is that the collective misalignment arises because of the excitation of the transverse phonon branch in the xy plane, which lies lower in energy than the longitudinal branch. This static distortion, which results in an increased internal energy of the adsorbate layer, is counterbalanced by a better interdigititation of the two lattices, that is, the displaced atoms are locally displaced to an overall more favorable stacking, with respect to the interlayer potential.^{41,42} If out-of-plane distortions, unaccounted for in the NM theory, lead to a better interplay between the two layers, that is, if there is a gain in the interlayer coupling energy that is larger than the intralayer energy penalty from out-of-plane modulations, the system will lower its total energy. Different from the NM theory, the lowest-energy distortion in this scenario would not result in a misalignment between the components but in the formation of ripples, creating locally commensurate zones at the equilibrium distance and incommensurate zones at a larger interlayer distance.

Here, we characterize the out-of-plane deformations, disregarded in NM theory, in terms of the flexural phonon branch, which describes excitations perpendicular to the ML plane. In line with our edge-free geometries, the phonon picture is independent of sample size, and because the phonon eigenvectors represent a complete basis set,⁴⁵ any distortion in the crystal may be expressed as a linear combination of phonons. Moreover, treating the distortions of a layer in terms of its phonon spectrum decouples the intralayer energetics from interlayer interaction. Our analysis, reported in section seven of the Supporting Information, shows that deformations in the MoS₂ ML are 2 orders of magnitude smaller than the deformation of G. This signals that the distortion governing the energy economy of the system happens in the G layer, and we therefore focus the following analysis on this part only. As shown by the blue solid line in Figure 4, the flexural band is flat near the center of the Brillouin zone (BZ) (Γ point), that is, the long-wave modulations perpendicular to the basal plane can occur essentially without an energy penalty. Transverse (dashed gray in Figure 4) and longitudinal (dash-dotted gray in Figure 4) bands, which are the basis of NM theory, are higher in energy, resulting in more expensive modulations of the G layer.

Although the phonon spectrum describes the energy penalty compared to an isolated ML at equilibrium, the energy gain from interlayer interactions can be quantified in terms of moiré patterns. The moiré superlattice is a geometrical construction

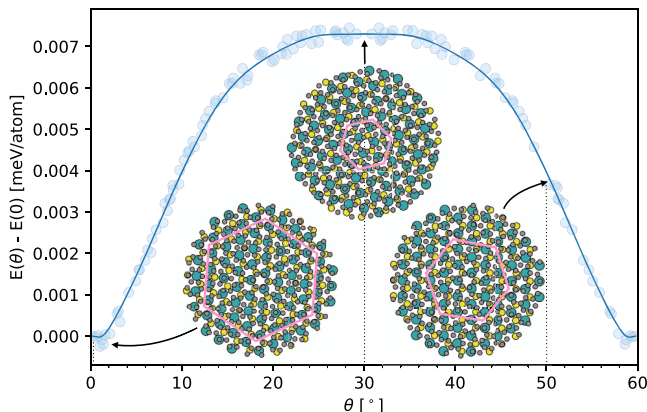


Figure 3. Energy per atom $E(\theta)$, in meV, as a function of the imposed angle θ . Each point in the energy landscape represents a distinct geometry at a different imposed angle, and the blue line is a Bézier fit. The small oscillations at $\theta = 0^\circ, 60^\circ$ are due to numerical noise in the energy simulations. The circular insets show top views of the relaxed structures at $\theta \approx 0^\circ$ (bottom left), $\theta \approx 50^\circ \equiv 10^\circ$ (bottom right), and $\theta \approx 30^\circ$ (top center). The atoms are colored according to the scheme in Figure 1. The pink hexagons sketch the moiré tile in each configuration.

angle θ (°) of the system without rigid substrate, but with two soft, interacting layers. Naturally, the LJ coupling between the two layers has been restored to the values obtained from fitting against the DFT data to correctly reproduce interlayer forces. The behavior that we found is both quantitatively and qualitatively different from the constrained system presented previously. The introduction of the out-of-plane dimension (z) changes the response qualitatively. The energy minima at nonzero angles have disappeared, and the energy now increases symmetrically from the global minima at the aligned cases

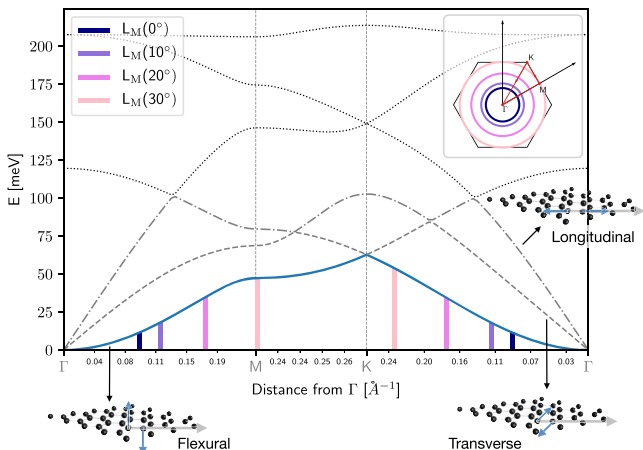


Figure 4. Phonon band structure of the G monolayer. The y axis reports the phonon energy, while the x axis marks the distance from the origin along the path $\Gamma \rightarrow M \rightarrow K \rightarrow \Gamma$, shown in the top right inset and marked along the x axis by gray dashed lines. The flexural branch is reported by a solid blue line, the transverse branch by is reported by a dashed gray line, and the longitudinal branch is reported by a dash-dotted gray line, while other branches are shown in dotted black lines. Colored segments along x increasing from $y = 0$ to the flexural branch mark wavevectors matching the moiré spacing $L_M(\theta)$ for the geometries in the insets of Figure 5, as highlighted by the color code. The moiré wavevector k_M corresponding to real-space wavelength L_M is shown in the top-right inset following the color code in the legend in the top left. The insets marked by black arrows show the characteristic displacement pattern for the three acoustic branches: the gray arrow indicates the direction of the wavevector \vec{k} and the blue arrow indicates the displacement of the atoms in a unit cell.

describing the interference between two lattices and can be used to identify geometrical correspondence between lattices, that is, zones of local commensuration versus incoherent stacking. The symmetry of the moiré superlattice reflects the one underlying Bravais lattices, and its lattice parameter L_M is given by⁴⁶

$$L_M(\theta) = \frac{l_G}{\sqrt{1 + \rho^{-2} - 2\rho^{-1}\cos\theta}} \quad (5)$$

Figure 5 shows the correlation between out-of-plane modulations, that is, rippling in the z dimension, and the moiré pattern in the G sheet. At $\theta = 0$, the moiré spacing and the average displacement along z are at a maximum, and they both decrease as the misalignment increases. As θ increases, the length of the pattern shrinks with the displacement along z : at $\theta = 30^\circ$, the moiré shrinks to a couple of unit cells and the monolayer remains basically flat. The rippling patterns follow the moiré superlattice perfectly, as shown in the insets of Figure 5 for selected values of θ , that is, the nearest configurations having approximately angles of $\theta = 0^\circ$ (0.23°), 10° (9.75°), 20° (19.89°), and 30° (29.17°). The local information expressed in the ripples of the carbon sheet is condensed in the thickness of the G layer

$$\tau(\theta) = \max_{\vec{r}_i \in G} z_i - \min_{\vec{r}_i \in G} z_i \quad (6)$$

which is a global parameter with a single value for each twisted geometry, as reported by black circles on the left y axis in Figure 5.

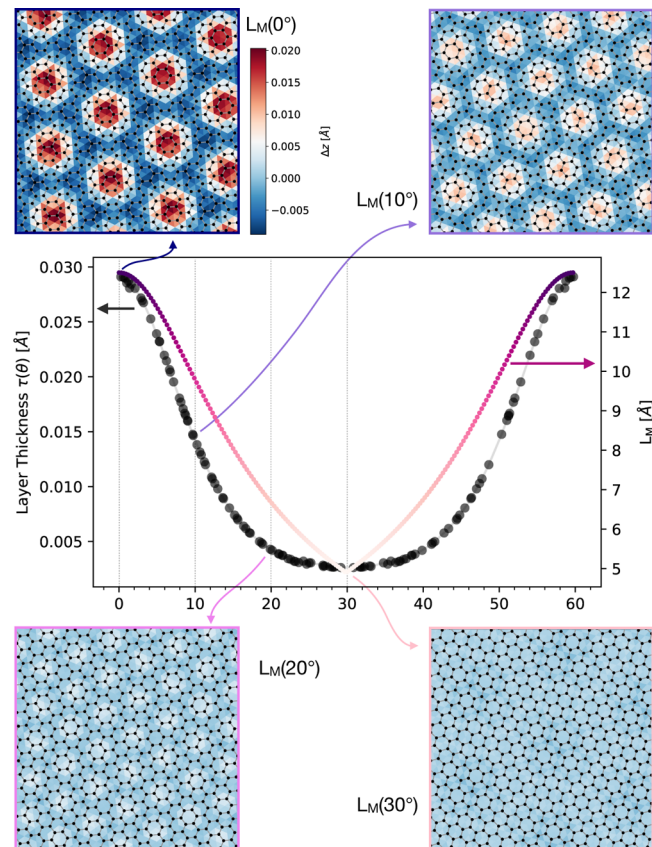


Figure 5. Thickness of the G layer $\tau(\theta)$ resulting from the displacement of C atoms (black circles, left axis) and spacing of the moiré pattern $L_M(\theta)$ (colored dotted line, right axis) as a function of θ for equivalent configurations at 0 and 60° rotating toward 30° . The insets show the local distortion following the moiré lattice in a square of sides 60 \AA at the nearest configuration having approximately angles of $\theta = 0^\circ$ (0.23° , dark purple), 10° (9.75° , purple), 20° (19.89° , dark pink), and 30° (29.17° , pink). The color of each triangle reports change in height $\Delta z = z - z_{eq}$ coordinate of the corresponding C atom (black points) following the color code reported in the top left. For example, the moiré pattern can be seen in the inset for $L_M(0^\circ)$ as the lattice defined by the red regions.

Combining the geometrical construction shown in Figure 5 and the G phonon dispersion in Figure 4, we can explain the energy profile in Figure 3. The moiré spacing $L_M(\theta)$ can be mapped to wavevectors into the BZ by $k_M(\theta) = \frac{2}{\sqrt{3}L_M(\theta)}$. The wavevectors k_M , corresponding to the spacing L_M of the geometries in the insets of Figure 5, are highlighted in Figure 4. All wavevectors in the BZ at the moiré spacing are shown by vertical segments along the path and as circles in the inset and follow the same color code. A modulation of the G sheet, with wavelength $L_M(\theta)$, can be represented as a combination of phonon modes of matching wavevectors $k_M(\theta)$. Because the modulation of the G layer essentially takes solely place in the z direction, the major contribution in the decomposition on phonon modes will come from the flexural branch. Within small displacements from the equilibrium positions, the energy price of such modulations can be estimated by the corresponding phonon energy. As θ varies from 0 to 30° and the moiré shrinks, like is shown in Figure 5, the associated wavevector $k_M(\theta)$ assumes the values between $k_M(0^\circ) = 0.09 \text{ \AA}^{-1}$ (dark-purple lines in Figure 4) and $k_M(30^\circ) = 0.24 \text{ \AA}^{-1}$ (pink lines in Figure 4), at increasing flexural-phonon energies.

Next, we describe these limiting cases in more detail. At $\theta = 0^\circ$, the spacing of the moiré is $L_M = 12.5 \text{ \AA}$, which is the distance between the locally commensurate patches, the red regions in Figure 5. As signaled by the dark-purple line in Figure 4, flexural phonon modes of this length in G are close to the flat region around Γ and therefore energetically inexpensive. This allows commensurate regions to stay at the equilibrium interlayer position, while incommensurate ones are pushed away from MoS₂ ML, perpendicular to the basal planes. As θ increases to 30° , L_M decreases, and thus, the distance between locally commensurate areas reduces. As a result, the deformation needs to occur over a shorter distance, and its energy cost therefore increases. At $\theta = 30^\circ$, $L_M = 4.88 \text{ \AA}$, which is about two G unit cells. As shown by the pink line in Figure 4, deformations of this length scale are described by phonons at the edges of the BZ and are energetically more expensive than the gain coming from the interdigititation with the substrate. Therefore, the G sheet remains flat, at the expense of the interlayer coupling, resulting in a higher total energy of the heterostructure compared to the aligned case. The flattening of the flexural branch near the edges of the BZ, as shown by the solid blue line between M and K in Figure 4, is mirrored by the plateau in the energy profile in Figure 3 around $\theta = 30^\circ$: in the whole region, moiré modulations are too expensive and the system cannot obtain any energy gain.

To sum up, the unconstrained 3D heterostructure lowers its energy by out-of-plane distortions according to the moiré pattern. This is particularly evident at $\theta = 0$, where $L_M = 12.5 \text{ \AA}$: here, the flexural distortion is almost without any energy penalty and the system lowers its energy by improving the interdigititation between G and the MoS₂ layers. As θ increases, L_M decreases and the cost of the ripples overtakes the gain in energy because of local commensuration, yielding flat G and an increased total energy. Finally, the region of the BZ spanned by the moiré spacing as a function of θ (the region between purple and pink segments in Figure 4) shows that the approximation of the long wavelength used to derive eq 4 is unsuited in the large-mismatched heterostructures. Because of the fact that also phonon excitation near the border of the BZ is involved in the energy economy of the system, a modified epitaxy theory is needed in these cases to predict and to understand the phase stability of imposed twist angles.

CONCLUSIONS

We explored the stability of twisted vdW heterostructures. Although often overlooked, this phenomenon is of particular importance in the emerging field of twistronics, as it can be a decisive factor in the real-life application of such systems. The energy as a function of an imposed angle determines whether a device is at risk of rotating away from a prepared angle. Our analysis of MoS₂/G heterostructures helps to clarify the scattered experimental data. We find a single global minimum at $\theta = 0$ and 60° , that is, only epitaxial stacking is expected for the system at 0 K. However, experiments always present defects or intrinsic friction that might result in the emergence of activation energies, potentially trapping a system in a metastable (or even unstable) state. In the limit where such effects become negligible, that is, activation energy approaching zero, one would mostly observe heterostructures aligned at $\theta = 0$ and 60° and few 30° -rotated, in agreement with the results of Liu *et al.*²³ A possible experiment, to test the validity of our results, would be to perform a systematic repetition of the aforementioned experiments, focused upon reducing

deviations resulting from working conditions, for example, annealing temperature. We expect that the results of such an effort will confirm our findings: with a high enough annealing temperature and large enough flakes of significant quality, the bilayer system should be found in the aligned configuration, with possibly some outliers at around 30° .

The relevance of our results becomes clear when considering the fact that interesting physics is observed at certain unstable mismatch angles.²⁸ Our findings show that care must be taken when designing nanodevices as properties observed in studies at a specific angle might fade over time because of the system spontaneously rotating toward the real thermodynamic equilibrium. In fact, others¹⁹ also suggest that aligned structures are most suitable for optospintronic applications.

Finally, we explain the origin of the observed energy economy in terms of the interplay between flexural phonon modes of the pristine compounds and the moiré superlattice. This insight is general in nature and can be applied to all layered materials and heterostructures, serving as a design tool for twistronic devices. Stiffness in the out-of-plane direction should be considered as a critical property in the design of such devices. It is for example known that rippling can affect the Schottky junctions, which are directly related to the performance of optoelectronic devices such as photodetectors and solar cells.⁴⁷ Soft flexural phonon modes might be a lower energy route out of frustration than twisting, hindering the possibility of stable rotated configurations. Furthermore, our results show the need for a novel theory of epitaxy for layered materials, incorporating the flexural branches ignored in the NM theory and taking into account all phonon wavelengths. The insights presented here can serve as a starting point for developing such a theory of the epitaxial growth for vdW heterostructures.

METHODS

Classical MD all-energy minimizations of the rotated heterostructures have been performed using molecular dynamics by means of the LAMMPS package⁴⁰ using the conjugate gradient algorithm, where the energy tolerance was set to 1×10^{-15} . The REBO potential³⁴ was used for G, whereas an adapted version of the three-body SW potential³³ was used for MoS₂. To model the vdW interactions, we used an interlayer LJ potential. To obtain the explicit values of the parameters, we refined the values that can be found in the paper by Ding *et al.*,³³ of which we provide an elaborate description in the Supporting Information.

DFT ab initio calculations used to reparametrize the force field were carried out using DFT as implemented in the VASP^{35,36} within the PAW framework.³⁷ The exchange–correlation potential is approximated using the PBE functional,³⁸ and the vdW dispersion is described by the DFT-D2 method.³⁹ A plane wave cutoff of 800 eV is adopted, and the BZ was sampled using a $13 \times 13 \times 1$ mesh.

Phonon calculation phonon bands were computed with the aid of Phonopy,⁴⁸ which was coupled to LAMMPS using phono-LAMMPS.⁴⁹ In both cases, the phonon dispersion was computed using the frozen method employing a $5 \times 5 \times 1$ supercell.

ASSOCIATED CONTENT

Supporting Information

The Supporting Information is available free of charge at <https://pubs.acs.org/doi/10.1021/acsami.0c13971>.

Details on the protocols, force field, and geometry parameters ([PDF](#))

AUTHOR INFORMATION

Corresponding Authors

Andrea Silva — *Engineering Materials, University of Southampton, Southampton SO17 1BJ, U.K.; national Centre for Advanced Tribology Study at University of Southampton, Southampton SO17 1BJ, U.K.*;  orcid.org/0000-0001-6699-8115; Email: a.silva@soton.ac.uk

Victor E. P. Claerbout — *Department of Control Engineering, Faculty of Electrical Engineering, Czech Technical University in Prague, Technicka 2, Prague 6 16627, Czech Republic;* Email: claervic@fel.cvut.cz

Authors

Tomas Polcar — *Engineering Materials, University of Southampton, Southampton SO17 1BJ, U.K.; Department of Control Engineering, Faculty of Electrical Engineering, Czech Technical University in Prague, Technicka 2, Prague 6 16627, Czech Republic*

Denis Kramer — *Engineering Materials, University of Southampton, Southampton SO17 1BJ, U.K.; Mechanical Engineering, Helmut Schmidt University, Hamburg 22043, Germany*

Paolo Nicolini — *Department of Control Engineering, Faculty of Electrical Engineering, Czech Technical University in Prague, Technicka 2, Prague 6 16627, Czech Republic;*  orcid.org/0000-0003-1324-7566

Complete contact information is available at:

<https://pubs.acs.org/10.1021/acsami.0c13971>

Author Contributions

A.S. and V.E.P.C. carried out all calculations and data analysis and conceptualize the study in the first place. P.N. and D.K. supervised extensively the study and T.P. guided the project. All authors contributed to the writing of this work. Finally, P.N., D.K., and T.P. secured funding acquisition.

Notes

The authors declare no competing financial interest.

ACKNOWLEDGMENTS

The authors are thankful to E. Tosatti, A. Vanossi, D. Mandelli, and M. Liao for the helpful discussions. This project has received funding from the European Union's Horizon2020 research and innovation programme under grant agreement no. 721642: SOLUTION. The authors acknowledge the use of the IRIDIS High Performance Computing Facility and associated support services at the University of Southampton in the completion of this work. This work was also supported by The Ministry of Education, Youth and Sports from the Large Infrastructures for Research, Experimental Development and Innovations project "e-Infrastructure CZ – LM2018140" and by the project Novel nanostructures for engineering applications no. CZ.02.1.01/0.0/0.0/16_026/0008396.

REFERENCES

- (1) Mannix, A. J.; Kiraly, B.; Hersam, M. C.; Guisinger, N. P. Synthesis and Chemistry of Elemental 2D Materials. *Nat. Rev. Chem.* **2017**, *1*, 0014.
- (2) Chhowalla, M.; Shin, H. S.; Eda, G.; Li, L.-J.; Loh, K. P.; Zhang, H. The Chemistry of Two-Dimensional Layered Transition Metal Dichalcogenide Nanosheets. *Nat. Chem.* **2013**, *5*, 263–275.
- (3) Vazirisereshk, M. R.; Martini, A.; Strubbe, D. A.; Baykara, M. Z. Solid Lubrication with MoS₂: A Review. *Lubricants* **2019**, *7*, 57.

- (4) Radisavljevic, B.; Radenovic, A.; Brivio, J.; Giacometti, V.; Kis, A. Single-Layer MoS₂ Transistors. *Nat. Nanotechnol.* **2011**, *6*, 147–150.
- (5) Lopez-Sanchez, O.; Lembke, D.; Kayci, M.; Radenovic, A.; Kis, A. Ultrasensitive Photodetectors Based on Monolayer MoS₂. *Nat. Nanotechnol.* **2013**, *8*, 497–501.
- (6) Lauritsen, J. V.; Bollinger, M. V.; Lægsgaard, E.; Jacobsen, K. W.; Nørskov, J. K.; Clausen, B. S.; Topsøe, H.; Besenbacher, F. Atomic-Scale Insight into Structure and Morphology Changes of MoS₂ Nanoclusters in Hydrotreating Catalysts. *J. Catal.* **2004**, *221*, 510–522.
- (7) Shi, X.-R.; Jiao, H.; Hermann, K.; Wang, J. CO Hydrogenation Reaction on Sulfided Molybdenum Catalysts. *J. Mol. Catal. A: Chem.* **2009**, *312*, 7–17.
- (8) Shi, X.-R.; Wang, S.-G.; Hu, J.; Wang, H.; Chen, Y.-Y.; Qin, Z.; Wang, J. Density Functional Theory Study on Water-Gas-Shift Reaction over Molybdenum Disulfide. *Appl. Catal., A* **2009**, *365*, 62–70.
- (9) Dienwiebel, M.; Verhoeven, G. S.; Pradeep, N.; Frenken, J. W. M.; Heimberg, J. A.; Zandbergen, H. W. Superlubricity of Graphite. *Phys. Rev. Lett.* **2004**, *92*, 126101.
- (10) Vazirisereshk, M. R.; Ye, H.; Ye, Z.; Otero-de-la-Roza, A.; Zhao, M.-Q.; Gao, Z.; Johnson, A. T. C.; Johnson, E. R.; Carpick, R. W.; Martini, A. Origin of Nanoscale Friction Contrast between Supported Graphene, MoS₂, and a Graphene/MoS₂ Heterostructure. *Nano Lett.* **2019**, *19*, 5496–5505.
- (11) Geim, A. K.; Grigorieva, I. V. Van der Waals Heterostructures. *Nature* **2013**, *499*, 419–425.
- (12) Novoselov, K. S.; Mishchenko, A.; Carvalho, A.; Castro Neto, A. H. 2D Materials and van der Waals Heterostructures. *Science* **2016**, *353*, aac9439.
- (13) Liu, Y.; Weiss, N. O.; Duan, X.; Cheng, H.-C.; Huang, Y.; Duan, X. Van der Waals Heterostructures and Devices. *Nat. Rev. Mater.* **2016**, *1*, 16042.
- (14) Zhang, K.; Fang, X.; Wang, Y.; Wan, Y.; Song, Q.; Zhai, W.; Li, Y.; Ran, G.; Ye, Y.; Dai, L. Ultrasensitive Near-Infrared Photodetectors Based on a Graphene-MoTe₂-Graphene Vertical van der Waals Heterostructure. *ACS Appl. Mater. Interfaces* **2017**, *9*, 5392–5398.
- (15) Zhu, S.; Pochet, P.; Johnson, H. T. Controlling Rotation of Two-Dimensional Material Flakes. *ACS Nano* **2019**, *13*, 6925–6931.
- (16) Du, L.; Yu, H.; Liao, M.; Wang, S.; Xie, L.; Lu, X.; Zhu, J.; Li, N.; Shen, C.; Chen, P.; Yang, R.; Shi, D.; Zhang, G. Modulating PL and Electronic Structures of MoS₂/Graphene Heterostructures via Interlayer Twisting Angle. *Appl. Phys. Lett.* **2017**, *111*, 263106.
- (17) Huang, Y. L.; Chen, Y.; Zhang, W.; Quek, S. Y.; Chen, C.-H.; Li, L.-J.; Hsu, W.-T.; Chang, W.-H.; Zheng, Y. J.; Chen, W.; Wee, A. T. S. Bandgap Tunability at Single-Layer Molybdenum Disulphide Grain Boundaries. *Nat. Commun.* **2015**, *6*, 6298.
- (18) Martin, J. M.; Erdemir, A. Superlubricity: Friction's Vanishing Act. *Phys. Today* **2018**, *71*, 40–46.
- (19) Du, L.; Zhang, Q.; Gong, B.; Liao, M.; Zhu, J.; Yu, H.; He, R.; Liu, K.; Yang, R.; Shi, D.; Gu, L.; Yan, F.; Zhang, G.; Zhang, Q. Robust spin-valley polarization in commensurate MoS₂/graphene heterostructures. *Phys. Rev. B* **2018**, *97*, 115445.
- (20) Zan, R.; Ramasse, Q. M.; Jalil, R.; Tu, J.-S.; Bangert, U.; Novoselov, K. S. Imaging Two Dimensional Materials and their Heterostructures. *J. Phys.: Conf. Ser.* **2017**, *902*, 012028.
- (21) Cao, Y.; Fatemi, V.; Fang, S.; Watanabe, K.; Taniguchi, T.; Kaxiras, E.; Jarillo-Herrero, P. Unconventional Superconductivity in Magic-Angle Graphene Superlattices. *Nature* **2018**, *556*, 43–50.
- (22) Liao, M.; Wu, Z.-W.; Du, L.; Zhang, T.; Wei, Z.; Zhu, J.; Yu, H.; Tang, J.; Gu, L.; Xing, Y.; Yang, R.; Shi, D.; Yao, Y.; Zhang, G. Twist Angle-Dependent Conductivities Across MoS₂/Graphene Heterojunctions. *Nat. Commun.* **2018**, *9*, 4068.
- (23) Liu, X.; Balla, I.; Bergeron, H.; Campbell, G. P.; Bedzyk, M. J.; Hersam, M. C. Rotationally Commensurate Growth of MoS₂ on Epitaxial Graphene. *ACS Nano* **2016**, *10*, 1067–1075.
- (24) Shi, Y.; Zhou, W.; Lu, A.-Y.; Fang, W.; Lee, Y.-H.; Hsu, A. L.; Kim, S. M.; Kim, K. K.; Yang, H. Y.; Li, L.-J.; Idrobo, J.-C.; Kong, J.

- Van der Waals Epitaxy of MoS₂ Layers Using Graphene As Growth Templates. *Nano Lett.* **2012**, *12*, 2784–2791.
- (25) Lu, C.-I.; Butler, C. J.; Huang, J. K.; Hsing, C. R.; Yang, H. H.; Chu, Y. H.; Luo, C. H.; Sun, Y. C.; Hsu, S. H.; Yang, K. H. O.; Wei, C. M.; Li, L. J.; Lin, M. T. Graphite Edge Controlled Registration of Monolayer MoS₂ Crystal Orientation. *Appl. Phys. Lett.* **2015**, *106*, 181904.
- (26) Adrian, M.; Senftleben, A.; Morgenstern, S.; Baumert, T. Complete Analysis of a Transmission Electron Diffraction Pattern of a MoS₂-Graphite Heterostructure. *Ultramicroscopy* **2016**, *166*, 9–15.
- (27) Diaz, H. C.; Avila, J.; Chen, C.; Addou, R.; Asensio, M. C.; Batzill, M. Direct Observation of Interlayer Hybridization and Dirac Relativistic Carriers in Graphene/MoS₂ van der Waals Heterostructures. *Nano Lett.* **2015**, *15*, 1135–1140.
- (28) Pierucci, D.; Henck, H.; Avila, J.; Balan, A.; Naylor, C. H.; Patriarche, G.; Dappe, Y. J.; Silly, M. G.; Sirotti, F.; Johnson, A. T. C.; Asensio, M. C.; Ouerghi, A. Band Alignment and Minigaps in Monolayer MoS₂-Graphene van der Waals Heterostructures. *Nano Lett.* **2016**, *16*, 4054–4061.
- (29) Naik, M. H.; Maity, I.; Maiti, P. K.; Jain, M. Kolmogorov-Crespi Potential for Multilayer Transition-Metal Dichalcogenides: Capturing Structural Transformations in Moiré Superlattices. *J. Phys. Chem. C* **2019**, *123*, 9770–9778.
- (30) Guerra, R.; van Wijk, M.; Vanossi, A.; Fasolino, A.; Tosatti, E. Graphene on h-BN: to Align or Not to Align? *Nanoscale* **2017**, *9*, 8799–8804.
- (31) Wang, Y.; Xiao, J.; Zhu, H.; Li, Y.; Alsaied, Y.; Fong, K. Y.; Zhou, Y.; Wang, S.; Shi, W.; Wang, Y.; Zettl, A.; Reed, E. J.; Zhang, X. Structural Phase Transition in Monolayer MoTe₂ Driven by Electrostatic Doping. *Nature* **2017**, *550*, 487–491.
- (32) Wang, Z.-J.; Ma, T.-B.; Hu, Y.-Z.; Xu, L.; Wang, H. Energy Dissipation of Atomic-scale Friction Based on One-Dimensional Prandtl-Tomlinson Model. *Friction* **2015**, *3*, 170–182.
- (33) Ding, Z.; Pei, Q.-X.; Jiang, J.-W.; Huang, W.; Zhang, Y.-W. Interfacial Thermal Conductance in Graphene/MoS₂ Heterostructures. *Carbon* **2016**, *96*, 888–896.
- (34) Brenner, D. W.; Shenderova, O. A.; Harrison, J. A.; Stuart, S. J.; Ni, B.; Sinnott, S. B. A Second-Generation Reactive Empirical Bond Order (REBO) Potential Energy Expression for Hydrocarbons. *J. Phys.: Condens. Matter* **2002**, *14*, 783–802.
- (35) Kresse, G.; Hafner, J. Ab Initio Molecular Dynamics for Open-Shell Transition Metals. *Phys. Rev. B: Condens. Matter Mater. Phys.* **1993**, *48*, 13115–13118.
- (36) Kresse, G.; Joubert, D. From Ultrasoft Pseudopotentials to the Projector Augmented-Wave Method. *Phys. Rev. B: Condens. Matter Mater. Phys.* **1999**, *59*, 1758–1775.
- (37) Blöchl, P. E. Projector Augmented-Wave Method. *Phys. Rev. B: Condens. Matter Mater. Phys.* **1994**, *50*, 17953–17979.
- (38) Perdew, J. P.; Burke, K.; Ernzerhof, M. Generalized Gradient Approximation Made Simple. *Phys. Rev. Lett.* **1996**, *77*, 3865–3868.
- (39) Grimme, S. Semiempirical GGA-type Density Functional Constructed with a Long-Range Dispersion Correction. *J. Comput. Chem.* **2006**, *27*, 1787–1799.
- (40) Plimpton, S. Fast Parallel Algorithms for Short-Range Molecular Dynamics. *J. Comput. Phys.* **1995**, *117*, 1–19.
- (41) Novaco, A. D.; McTague, J. P. Orientational Epitaxy-The Orientational Ordering of Incommensurate Structures. *Phys. Rev. Lett.* **1977**, *38*, 1286–1289.
- (42) McTague, J. P.; Novaco, A. D. Substrate-Induced Strain and Orientational Ordering in Adsorbed Monolayers. *Phys. Rev. B: Condens. Matter Mater. Phys.* **1979**, *19*, 5299–5306.
- (43) Brazda, T.; Silva, A.; Manini, N.; Vanossi, A.; Guerra, R.; Tosatti, E.; Bechinger, C. Experimental Observation of the Aubry Transition in Two-Dimensional Colloidal Monolayers. *Phys. Rev. X* **2018**, *8*, 011050.
- (44) Panizon, E.; Guerra, R.; Tosatti, E. Ballistic Thermophoresis of Adsorbates on Free-Standing Graphene. *Proc. Natl. Acad. Sci. U.S.A.* **2017**, *114*, E7035–E7044.
- (45) Wallace, D. C.; Callen, H. Thermodynamics of Crystals. *Am. J. Phys.* **1972**, *40*, 1718–1719.
- (46) Mandelli, D.; Vanossi, A.; Manini, N.; Tosatti, E. Friction Boosted by Equilibrium Misalignment of Incommensurate Two-Dimensional Colloid Monolayers. *Phys. Rev. Lett.* **2015**, *114*, 108302.
- (47) Tomer, D.; Rajput, S.; Li, L. Spatial inhomogeneity in Schottky barrier height at graphene/MoS₂ Schottky junctions. *J. Phys. D: Appl. Phys.* **2017**, *50*, 165301.
- (48) Togo, A.; Tanaka, I. First Principles Phonon Calculations in Materials Science. *Scr. Mater.* **2015**, *108*, 1–5.
- (49) Carreras, A. phonoLAMMPS. <https://github.com/abelcarreras/phonolammps>, 2019.